ChemComm

HIGHLIGHT

View Article Online
View Journal | View Issue

Cite this: *Chem. Commun.*, 2024, **60**, 5232

Recent advances in electrosynthesis of H_2O_2 *via* two-electron oxygen reduction reaction

Ao Yu,[a] Shengwen Liu[a] and Yang Yang *[abcde]

Received 31st March 2024,
Accepted 17th April 2024

DOI: 10.1039/d4cc01476f

rsc.li/chemcomm

The electrosynthesis of hydrogen peroxide (H_2O_2) *via* a selective two-electron oxygen reduction reaction ($2e^-$ ORR) presents a green and low-energy-consumption alternative to the traditional, energy-intensive anthraquinone process. This review encapsulates the principles of designing relational electrocatalysts for $2e^-$ ORR and explores remaining setups for large-scale H_2O_2 production. Initially, the review delineates the fundamental reaction mechanisms of H_2O_2 production *via* $2e^-$ ORR and assesses performance. Subsequently, it methodically explores the pivotal influence of microstructures, heteroatom doping, and metal hybridization along with setup configurations in achieving a high-performance catalyst and efficient reactor for H_2O_2 production. Thereafter, the review introduces a forward-looking methodology that leverages the synergistic integration of catalysts and reactors, aiming to harmonize the complementary characteristics of both components. Finally, it outlines the extant challenges and the promising avenues for the efficient electrochemical production of H_2O_2, setting the stage for future research endeavors.

1. Introduction

Hydrogen peroxide (H_2O_2) is one of the most significant industrial chemicals all over the world, with a wide range of applications that extend from paper and textile manufacturing to wastewater treatment systems, polymer and pharmaceutical syntheses, and organic degradation due to its remarkable oxidative and environmentally benign properties.[1–5] However, 95% of the H_2O_2 product is produced by the anthraquinone oxidation (AO) process, which requires the presence of a noble palladium catalyst, hydrogenation, and oxidation steps (Fig. 1a), along with the recycling of excessive organic solvent and distillation of H_2O_2 from the reaction mixture.[6,7] These disadvantages result in high costs, excessive energy consumption, and multiple operations. These limitations have prompted researchers to investigate alternative, environmentally friendly technologies for synthesizing H_2O_2. A notable alternative to the conventional AO approach for manufacturing H_2O_2 is the direct synthesis process, which utilizes hydrogen (H_2) and oxygen (O_2) as the initial reactants (Fig. 1b). This method employs a catalytic reaction, typically mediated by palladium/platinum (Pd/Pt) or similar catalysts, to combine these gases directly into H_2O_2 under carefully managed conditions. However, the direct synthesis of H_2O_2 (DS-H_2O_2) utilizing H_2 and O_2 faces several challenges, including the inherent safety risks due to the explosive nature of the H_2 and O_2 reaction, lower yields which reduce efficiency, the necessity for costly noble metal catalysts, operational complexities requiring precise control over reaction conditions to maintain selectivity, and generally lower production rates that may not meet industrial-scale demands.[8–10] Therefore, to facilitate widespread adoption, it is essential to develop other efficient and cost-effective methods for the synthesis of H_2O_2.

Notably, the electrochemical approach, utilizing the two-electron oxygen reduction reaction ($2e^-$ ORR) pathway, presents a promising method for generating H_2O_2. This technique is advantageous due to its portability and enhanced safety profile (Fig. 1c).[6] Additionally, the electrocatalytic 2-electron oxygen reduction reaction ($2e^-$ ORR) occurs in an aqueous electrolyte (for example, aqueous KOH, phosphate-buffered saline (PBS), H_2SO_4, $HClO_4$, and Na_2SO_4) with O_2 as the starting material.[11–15] This process avoids the use of excessive organic solvents required in the AO process and eliminates the direct contact between H_2 and O_2 in the DS-H_2O_2 process, indicating that it is more environmentally friendly and safer compared to the other two methods. Furthermore, the $2e^-$ ORR can be driven at low voltage, suggesting that it can be integrated with renewable energy sources. These advantages position it as a sustainable alternative to supersede both the AO and DS-H_2O_2 processes. In the $2e^-$ ORR, H_2O_2 is produced directly through the reduction of O_2 at the cathode.

[a] *NanoScience Technology Center, University of Central Florida, Orlando, FL, 32826, USA. E-mail: Yang.Yang@ucf.edu*
[b] *Department of Materials Science and Engineering, University of Central Florida, Orlando, FL 32826, USA*
[c] *Renewable Energy and Chemical Transformation Cluster, University of Central Florida, Orlando, FL 32826, USA*
[d] *Department of Chemistry, University of Central Florida, Orlando, FL 32826, USA*
[e] *The Stephen W. Hawking Center for Microgravity Research and Education, University of Central Florida, Orlando, FL 32826, USA*

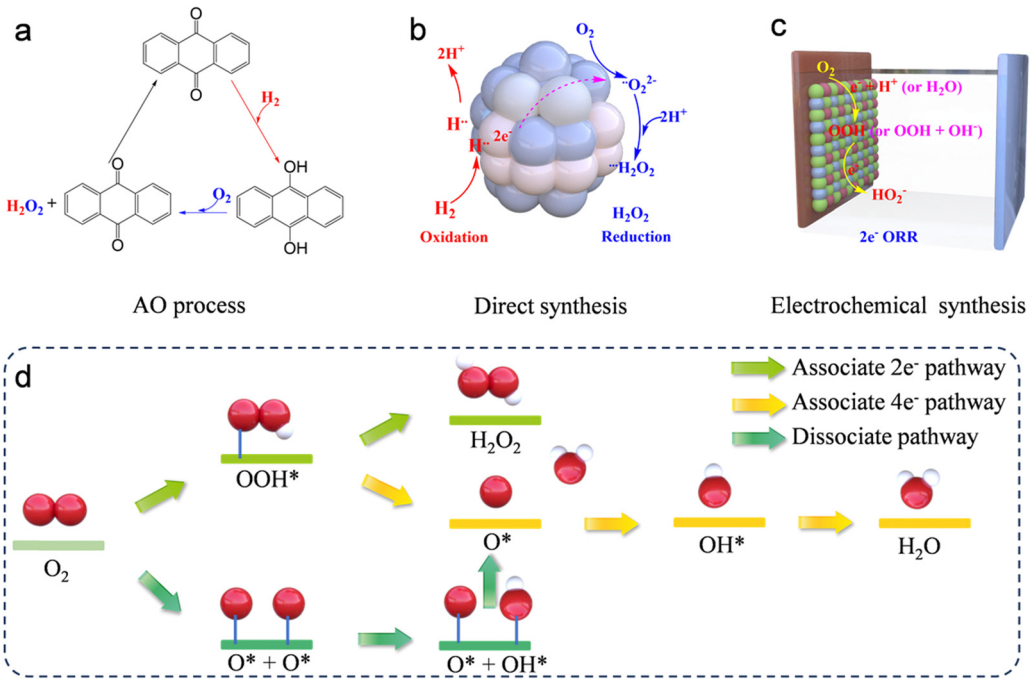

Fig. 1 Illustration of hydrogen peroxide production *via* (a) traditional anthraquinone process, (b) the direct synthesis, and (c) electrochemical two-electron oxygen reduction reaction. (d) Illustration of the proposed ORR process.

Notwithstanding the advantages, the sluggish reaction kinetics coupled with side reactions significantly impede the overall energy efficiencies. Consequently, the essential conditions for the optimization of H_2O_2 electrochemical synthesis involve the deliberate design of specialized catalysts. These catalysts must favor the selective $2e^-$ ORR pathway, while inhibiting the competing $4e^-$ ORR pathway, and should exhibit high activity, superior selectivity, and strong stability. To date, optimal practical outcomes in $2e^-$ ORR have been achieved through rational engineering of catalysts that offer affordability, abundance, and durability.[16–20] The engineering strategies involve microstructural engineering, heteroatom doping engineering, and metal hybridization engineering. Many recent studies have confirmed that the dimensions and types of pore structures significantly affect the $2e^-$ ORR performance.[19,21–24] For example, three-dimensional (3D) materials can effectively avoid stacked structures, thereby favoring the exposure of more catalytically active sites. The mesopore structure in the materials can reduce the retention time of H_2O_2 on the catalyst surface, thus enhancing the productivity of H_2O_2.[22,23] In addition to the influence of structure on the $2e^-$ ORR performance, the composition of the catalysts significantly impacts the performance. The doping of heteroatoms and metallic hybridization are subjects of extensive study because of the ability of heteroatom incorporation into substrates to activate otherwise inert atoms and the inherent high activity of metals in catalyzing the oxygen reduction reaction.[25] Moreover, given that the objective of the $2e^-$ ORR is to supplant the conventional AO process, the setups for large-scale H_2O_2 production assume critical importance. It is essential to design a logical setup that can maximize catalyst utilization and facilitate continuous production.

The exploration of electrochemical synthesis of H_2O_2 through a $2e^-$ ORR represents a burgeoning research domain. Despite the abundance of comprehensive reviews on the $2e^-$ ORR, the focus on integrating catalyst engineering involving basic design principles with existing large-scale setups for H_2O_2 production remains limited. This review discusses the reaction mechanisms, performance assessment, design principles of catalysts, and setups for large-scale H_2O_2 production.

2. Reaction mechanisms of H_2O_2 production *via* $2e^-$ ORR

In the cathode of an electrochemical cell, the electrochemical oxygen reduction reaction (ORR) can follow two distinct pathways in aqueous environments: $2e^-$ ORR and $4e^-$ ORR.[25–28] In the $2e^-$ ORR, H_2O_2 is the primary product, whereas in the $4e^-$ ORR, the final product is H_2O. These reactions are influenced by distinct catalysts and environmental conditions. Thus, the selection of the catalyst and reaction media play critical roles in determining the predominant reduction pathway. Typically, the ORR unfolds through either a dissociative or an associative pathway. The dissociative pathway involves breaking the O–O bond upon oxygen adsorption, leading to the formation of adsorbed oxygen (O), which is sequentially reduced to adsorbed hydroxide (OH_{ads}) and adsorbed water (H_2O_{ads}). Conversely, the associative mechanism retains the O–O bond, with the end products being either water (H_2O) or H_2O_2, contingent upon the capacity of the catalysts to split the O–O bond within the *OOH intermediate. Regarding H_2O_2 production *via* the $2e^-$ ORR, as illustrated in Fig. 1d, the O_2 molecule initially attaches to the active sites, undergoing

hydrogenation to form *OOH, which is finally reduced to H_2O_2. Conversely, if the O–O bond is broken, the resulting *O undergoes further reduction, leading to the unwanted formation of H_2O. Thus, preserving the O–O bond and fine-tuning the adsorption energy of *OOH are essential steps to maximize H_2O_2 yield. For an ideal $2e^-$ ORR catalyst, it is critical to strongly adsorb O_2 molecules to initiate *OOH formation. Moreover, the adsorption at active sites should be sufficiently weak to enable straightforward desorption of *OOH, leading to H_2O_2 production. In summary, the production of H_2O_2 through the $2e^-$ ORR is a dual-step hydrogenation process involving the generation of *OOH intermediates and H_2O_2 at active sites, see eqn (1) and (2).

$$* + O_2 + H^+ + e^- = *OOH \quad (1)$$

$$*OOH + H^+ + e^- = H_2O_2 + * \quad (2)$$

where * represents the active sites.

According to the discussion above, the adsorption energy of *OOH determines the $2e^-$ ORR pathway. The limiting potential (U_L) is defined as the minimal potential at which all steps of the reaction proceed in a thermodynamically favorable direction. Consequently, the theoretical overpotential can be determined by calculating the difference between the limiting potential and equilibrium potential.[29] The graphical representation of U_L *versus* (*vs.*) ΔG_{*OOH} for the $2e^-$ ORR demonstrates a volcanic shape. At the extreme left of the volcano plot, the *OOH intermediate exhibits overly strong adsorption to the active sites, steering the ORR mechanism towards a $4e^-$ process. This indicates a reduced selectivity for the $2e^-$ ORR pathway, albeit with elevated activity. Conversely, at the extreme right of the volcano plot, the *OOH intermediate on the surface of active sites exhibits insufficient surface binding, resulting in heightened selectivity for the $2e^-$ ORR pathway, albeit at the cost of diminished activity. Thus, to achieve optimal activity and selectivity for the $2e^-$ ORR, active sites should ideally be positioned near the peak of the volcano plot.

In addition, it should also be noted that the catalytic process of $2e^-$ ORR varies in different electrolytes. The half-cell reactions can be expressed as follows (eqn (3a) and (4a)).[30] However, studies on the H_2O_2 production mechanism in neutral electrolytes are scarce. In such electrolytes, both hydroxyl species and protons are sparse. Therefore, further investigation into the ORR pathway is necessary to uncover the impact of pH on H_2O_2 production. The occurrence of $2e^-$ ORR inevitably accompanies the $4e^-$ ORR, as shown in eqn (3b) and (4b).

$$\text{Acid media: } O_2 + 2H^+ + 2e^- = H_2O_2,\ E^0 = 0.70\ \text{V } \textit{vs.}\ \text{RHE at PH} < 11.6 \quad (3a)$$

$$O_2 + 4H^+ + 4e^- = 2H_2O,\ E^0 = 1.23\ \text{V } \textit{vs.}\ \text{RHE} \quad (3b)$$

$$\text{Basic media: } O_2 + 2H_2O + 2e^- = H_2O_2 + 2OH^-,\ E^0 = 0.74\ \text{V } \textit{vs.}\ \text{RHE at PH} = 13 \quad (4a)$$

$$O_2 + 2H_2O + 4e^- \rightarrow 4OH^-,\ E^0 = 1.23\ \text{V } \textit{vs.}\ \text{RHE} \quad (4b)$$

where E^0 represents the standard equilibrium potential, while RHE refers to the reversible hydrogen electrode.

3. Performance assessment: rotating-ring disk electrode and applicable devices

The utilization of the rotating ring-disk electrode (RRDE) technique constitutes a pivotal methodology in the comprehensive evaluation of H_2O_2 electrosynthesis and the elucidation of oxygen reduction reaction (ORR) mechanisms. This advanced approach enables the accurate determination of H_2O_2 yields resulting from the ORR by initially enabling the reduction of molecular O_2 at the disk electrode, thereby generating both H_2O and H_2O_2. Subsequently, the rotation of the disk electrode expedites the transfer of produced H_2O_2 to a platinum ring electrode, where H_2O_2 is oxidized back to O_2. This process facilitates the quantification of H_2O_2 through the generation of a measurable ring current. Elevated currents observed at the disk electrode are indicative of robust ORR activity, whereas augmented ring currents indicate significant H_2O_2 production, thereby evidencing the efficacy of H_2O_2 production. By assessing the currents measured at both the disk and ring electrodes, the number of electrons transferred (n) and the selectivity towards H_2O_2 production (%) can be meticulously calculated, as shown in eqn (5)–(7).

$$\text{Selectivity of } H_2O_2(\%) = \frac{200 \times I_{ring}}{N \times |I_{disk}| + I_{ring}} \quad (5)$$

$$\text{Electron transfer number}(n) = \frac{4 \times |I_{disk}|}{|I_{disk}| + I_{ring}/N} \quad (6)$$

$$H_2O_2\ \text{faradaic efficiency}(\%) = \frac{I_{ring}}{N \times I_{disk}} \quad (7)$$

where I_{ring}, I_{disk}, and N represent the ring current, disk current, and the collection efficiency of the RRDE, respectively. The n values approaching 2 indicate reactions predominantly following a two-electron pathway, resulting in H_2O_2 production, while n values nearing 4 imply the predominance of a four-electron pathway leading to the formation of H_2O. The applied potential on the ring electrode is set at 1.2 V (*vs.* RHE) to quantify the H_2O_2, where the H_2O_2 is oxidized back to O_2.[31]

The true efficiency of catalysts for H_2O_2 production can be assessed through electrolyzer setups. Such configurations provide a practical measure of H_2O_2 electrosynthesis performance, offering a more applicable comparison to the RRDE method. This approach allows for the evaluation of catalyst stability and the potential for large-scale production over prolonged periods. The concentration of H_2O_2 can be measured using conventional titration methods, such as $Ce(SO_4)_2$ titration or iodometric titration. The H_2O_2 concentration obtained in applicable devices can be ascertained through the transformation of yellow Ce^{4+} ions to colorless Ce^{3+} ions, facilitated by H_2O_2, allowing for the determination of H_2O_2 concentration based on the change in Ce^{4+} ion concentration before and after the reaction (see eqn (8)–(10)). In iodometric titration, the process involves the oxidation of I- ions into I_2 within an acidic environment. Following this, the introduction of a starch

aqueous solution to the solution containing I_2 results in the formation of a dark blue complex. To conclude the titration and evaluate the H_2O_2 concentration, $Na_2S_2O_3$ is gradually added to the dark blue mixture until the color vanishes (see eqn (11)–(13)).

$$2Ce^{4+} + H_2O_2 = 2Ce^{3+} + 2H^+ + O_2 \quad (8)$$

$$C_{H_2O_2} = \frac{V_{Ce^{4+}} \times C_{before}Ce^{4+} - \left(V_{Ce^{4+}} + V_{1,telectrolyte}\right) \times C_{after}Ce^{4+}}{2 \times V_{2,electrolyte}} \quad (9)$$

$$\text{Faraday efficiency}(\%) = \frac{2 \times C \times V \times F}{Q} \quad (10)$$

where $C_{H_2O_2}$ is the real H_2O_2 concentration in an applicable device, $V_{Ce^{4+}}$, $V_{1,telectrolyte}$, $C_{before}Ce^{4+}$ $C_{after}Ce^{4+}$, and $V_{2,electrolyte}$ represent the volume of the used $Ce(SO_4)_2$ solution, the volume of electrolyte taken from the electrolyzer, the initial concentration of $Ce(SO_4)_2$, the final concentration of $Ce(SO_4)_2$ after H_2O_2 is added, and the total electrolyte volume, respectively. In eqn (10), C represents the concentration of H_2O_2, V denotes the volume of the electrolyte, F stands for the Faraday constant (96 485 C mol^{-1}), and Q refers to the charge consumed.

$$H_2O_2 + 2KI + H_2SO_4 \rightarrow I_2 + K_2SO_4 + 2H_2O \quad (11)$$

$$I_2 + 2Na_2S_2O_3 \rightarrow Na_2S_4O_6 + 2NaI \quad (12)$$

$$\text{Faraday efficiency}(\%) = \frac{16Vc \times 96485}{Q} \times 100\% \quad (13)$$

where the V, c, and Q represent the consumed volume of $Na_2S_2O_3$, the concentration of $Na_2S_2O_3$, and the applied charge during the electrolysis, respectively.

4. Strategies to design catalysts for the 2e$^-$ ORR

4.1 Microstructure engineering

The engineering of microstructures of materials plays a vital role in boosting catalytic performance due to their influence on the specific surface area (SSA), exposure of catalytic active sites, mass diffusion, and conductivities. The microstructures are influenced by both their dimensions and porosities. Materials processing similar chemical compositions with different dimensions and porosities usually display completely different features in terms of catalytic performance. Therefore, understanding the effects of microstructures can lead to an effective material design. For example, three-dimensional (3D) materials predominantly contain porous structures including macropores, mesopores and micropores. Such controllable pore structures can purposely regulate the 2e$^-$ ORR coordination of reaction intermediates by changing the exposure of active sites and the retention time of H_2O_2 in the specialized pore size, thus determining the overall performance of a catalyst.[22,23] Regarding materials with two-dimensional (and one-dimensional) structures, such as graphene (and typical carbon nanotubes (CNTs)), they are distinguished by distinctive flake-like and linear morphologies, wherein the active sites are constituted by surface functional groups and/or structural defects. Furthermore, the two-dimensional (2D) and one-dimensional (1D) substrates serve as efficacious carriers for electron transfer processes. In this section, the effects of microstructures of materials regarding the dimensions and porosities on the 2e$^-$ ORR performance will be comprehensively discussed.

Regarding the materials with 3D structure and sufficient pore structure, the 2e$^-$ ORR performance of a material is affected by the SSA and types of pore structure in 3D materials, as shown in Fig. 2a. Chai *et al.* reported the synthesis of mesoporous carbon hollow spheres exhibiting an exceptionally high specific surface area (SSA) of 1362.4 $m^2\ g^{-1}$. These spheres displayed a remarkably high selectivity for H_2O_2 production, reaching 99.9% in a neutral phosphate-buffered saline (PBS) electrolyte,[19] as shown in Fig. 2d. The unique hollow morphology and the structural features of the radial channels contribute to an increased SSA, which in turn facilitates mass transfer during the oxygen reduction reaction process. In an analogous research, a hierarchically porous carbon material was developed, boasting an ultrahigh SSA exceeding 2500 $m^2\ g^{-1}$. It is claimed that the SSA plays a pivotal role in enhancing the performance of H_2O_2 production.[21] The optimal porous architecture enhances the exposure of electroactive sites, thereby augmenting the utilization efficiency of these sites for H_2O_2 production. Therefore, the 3D structure with high SSA is beneficial for both exploring the actives and accelerating the mass transfer for H_2O_2 production. The inherent relation between the structural features and H_2O_2 production performance is deeply studied by analyzing the states of H_2O_2 in the pore structure because materials processing high SSA include macropores, mesopores and micropores. In the realm of catalysis, the presence of mesopore structures within catalysts significantly accelerates the migration route of H_2O_2 due to enhanced mass transport capabilities, in contrast to the restricted mobility inherent in micropore structures.[22,23] This phenomenon is illustrated in Fig. 2b and c: the H_2O_2 generated in the mesopore structure can easily diffuse into the bulk electrolyte, reducing the decomposition of H_2O_2 and thus enhancing the production. However, in micropore structures, H_2O_2 is either transiently held within micropores or compelled to traverse extended distances to reach the catalyst surface. This distinct discrepancy between mesopore and micropore configurations markedly influences the residency duration of H_2O_2 within the catalyst structure. For example, nitrogen-doped carbons with a mesoporous architecture reveal a notable H_2O_2 selectivity exceeding 90% in acidic electrolytes. Such remarkable H_2O_2 selectivity can be attributed to the fast mass transfer and minimized contact time of H_2O_2 within these mesoporous structures.[22] In another research, Chuanxin He *et al.* highlighted that micro/mesoporous carbon architectures can elevate the local pH and expedite the generation of intermediates (*O_2 and *OOH) *via* inducing a localized pseudo-alkaline environment, thereby enhancing the efficiency of H_2O_2 production.[32]

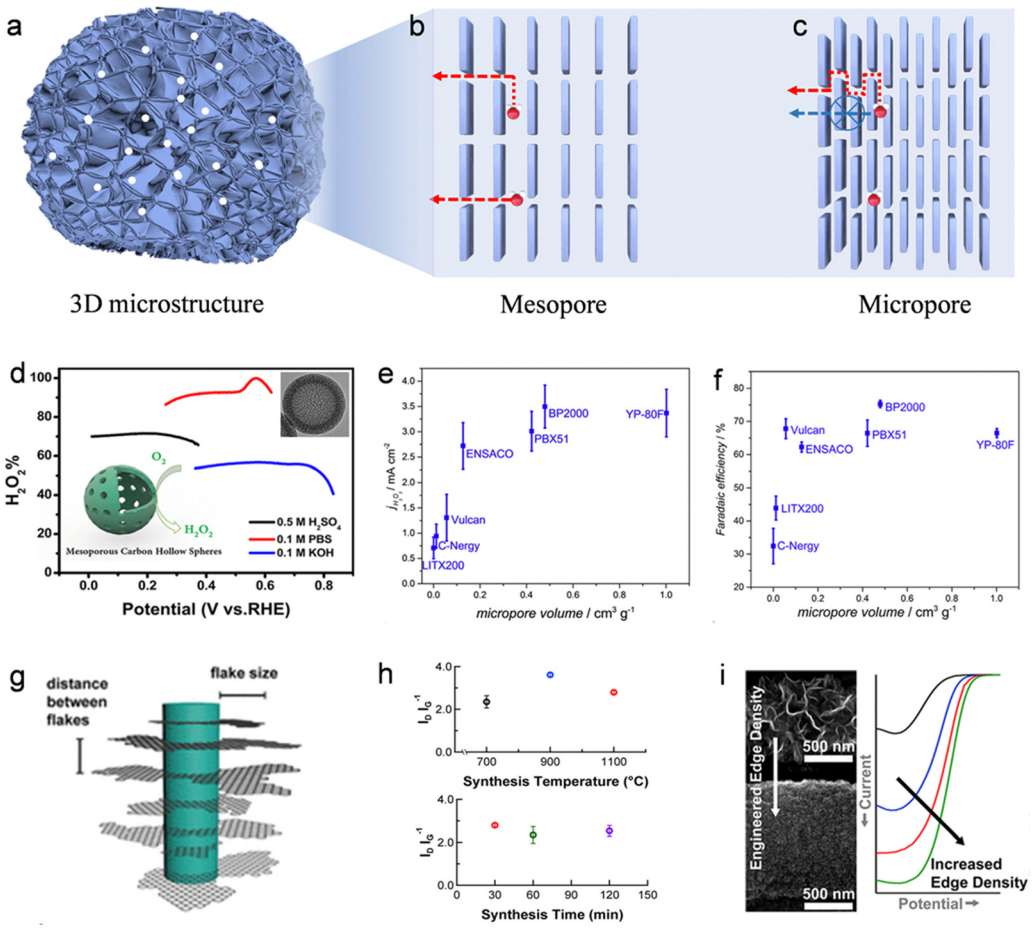

Fig. 2 Schematic of the (a) 3D microstructure, (b) mesopore and (c) micropore. (d) H_2O_2 selectivity of mesoporous carbon hollow spheres. Reproduced from ref. 22. Copyright (2014) American Chemical Society. (e) Current densities of H_2O_2 and (f) faradaic efficiency as a function of micropore volume. Reproduced from ref. 24. Copyright (2018) Elsevier. (g) Ordered structure of graphene flakes on carbon nanowires. (h) Representative Raman spectra of NT-3DFGs. (i) SEM image and representative rotating disk electrode linear sweep voltammetry (LSV) curves (n = 3) for glassy carbon (black) and NT-3DFGs. Reproduced from ref. 34.Copyright (2020) American Chemical Society.

Furthermore, the pore volume also plays a crucial role in determining the selectivity towards H_2O_2 production in the 2e$^-$ ORR. As documented in Fig. 2e and f, Chorkendorff and colleagues elucidated that carbon materials endowed with substantial microporous volumes manifest a pronounced selectivity for H_2O_2 production.[24] Specifically, Fig. 2e and f demonstrate an increase in H_2O_2 current density concomitant with the augmentation of micropore volume, underscoring the beneficial impact on 2e$^-$ ORR efficiency. The production volume of H_2O_2 is positively correlated with the extent of microporous volume, implying that these micropores act as auxiliary active sites, enhancing the catalytic process.

In addition to the SSA and pore structure, microstructural engineering also involves the design of geometrical structures, which is mainly related to the rational utilization of active sites. As shown in Fig. 2g, both commonly used graphene and CNTs, when utilized as 2e$^-$ ORR catalysts, are functionalized with active epoxy, hydroxyl, carbonyl groups, and the defects.[2,11–13,33] The rational design of ordered microstructures has been regarded as an effective strategy to improve the H_2O_2 production in 2e$^-$ ORR by taking full advantage of the edge sites with functional groups. A graphene-based hybrid nanomaterial, known as nanowire-templated out-of-plane three-dimensional fuzzy graphene (NT-3DFG), has been developed.[34] This material is characterized by its unique arrangement of independent graphene layers on nanowires, as depicted in Fig. 2g. The innovative composite structure not only prevents the graphene layers from stacking but also significantly enhances the accessibility of the edge sites on graphene flakes. Adjusting the density of these out-of-plane graphene flakes by simply changing the annealing temperature and time (Fig. 2h) allows for the modulation of both the density of active sites for ORR and the overall ORR activity of NT-3DFG. The finely regulated NT-3DFG sample exhibits exceptional 2e$^-$ ORR performance, including an onset potential of 0.79 ± 0.01 V *vs.* RHE and a high selectivity for hydrogen peroxide production (94 ± 2% H_2O_2). Thanks to the optimized arrangement of vertically aligned graphene on nanowires, the limiting current density for the oxygen reduction reaction experienced an enhancement, concurrent with the increase in edge density (Fig. 2i).

4.2 Heteroatom doping engineering

Heteroatom doping engineering involves introducing alloplastic atoms into an inert substrate, which can regulate the local electronic structure to activate the inert atoms, thus enhancing the catalytic activity.[25] In addition, heteroatoms can also introduce active functional groups, which function as active sites for 2e$^-$ ORR, into the substrate to achieve a high-performance catalyst, such as the oxygen-bearing functional groups on the carbon-based materials. Generally, heteroatom doping engineering involves doping non-metallic/metallic heteroatoms into carbonaceous/non-carbonaceous materials. Regarding the heteroatom-doped carbonaceous materials, elements such as boron (B), nitrogen (N), oxygen (O), fluorine (F), phosphorous (P), and sulfur (S) are doped into carbon substrates to activate the electrochemically inactive atoms by regulating the electronic conductivity or introducing defect sites.[7,35,36]

Great attention has been paid to the oxygen-doped carbonaceous materials (O–C). The oxygen incorporation into carbons can greatly localize the π electron distribution, achieving high H_2O_2 selectivity towards the 2e$^-$ ORR, while the activity of O–C is limited because of the high resistance of surface charge transfer. Studies on the effects of oxygen dopants on the 2e$^-$ ORR mainly focus on identifying the specific oxygen-bearing functional groups. As reported in numerous works, as shown in Fig. 3a, the quinone functions, carbonyl, and ether/epoxy can

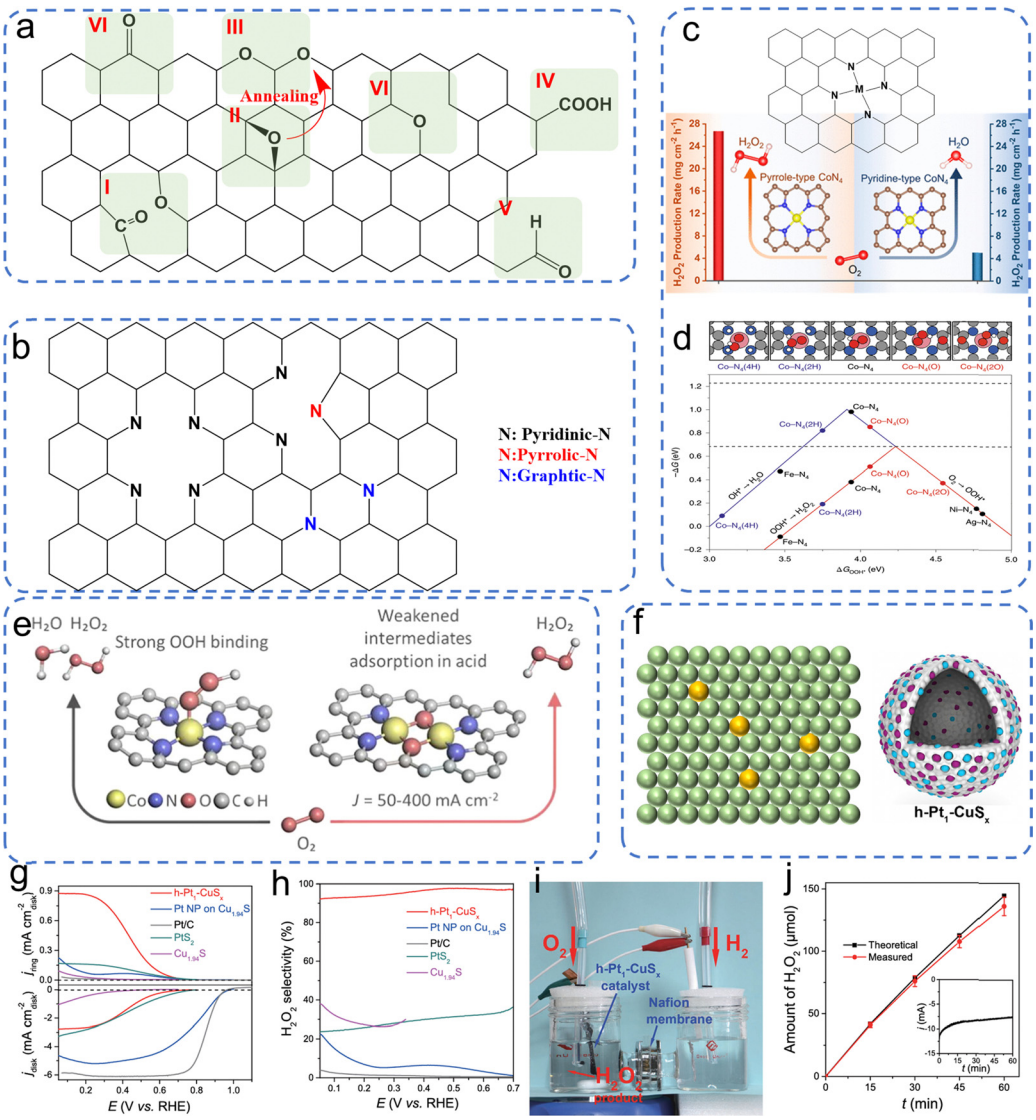

Fig. 3 Illustration of (a) oxygen dopant, (b) nitrogen dopant and (c) metal–N*x* site on a graphene substrate. Reproduced from ref. 52. Copyright (2022) American Chemical Society. (d) DFT calculations of different metal–N*x* sites on the volcano plot. Reproduced from ref. 51. Copyright (2020) Springer Nature. (e) Illustration of diatomic cobalt sites on a carbon substrate. Reproduced from ref. 57. Copyright (2024) American Chemical Society. (f) Illustration of atomically dispersed metallic atoms on non-carbonaceous substrates and schematic representation of the structural evolution of h-Pt1-CuS_x. (g) Linear sweep voltammetry (LSV) curves were obtained utilizing a rotating ring-disk electrode (RRDE) in an electrolyte solution of 0.1 M O_2-saturated $HClO_4$. (h) The selectivity towards H_2O_2. (i) The electrochemical device employed for the electrosynthesis of H_2O_2. (j) The quantification of H_2O_2 produced over time. Reproduced from ref. 20. Copyright (2019) Elsevier.

function as active sites for the 2e$^-$ ORR.[13,17,28,37–39] Typically, the catalytic activities of these oxygen-bearing groups are different in various chemical coordination environments. For example, when oxygen atoms were introduced into carbon to prepare quinone-rich, carbonyl-rich, and etheric-rich carbon,[38] the quinone functional groups, as shown in Fig. 3a (area I), were confirmed as the most active site compared to the other oxygen groups. More importantly, the catalytic activity of an oxygen group is highly dependent on the geometric position. For example, the C–O groups located at the base of few-layered mildly reduced graphene oxide (mrGO) gradually transform into ordered arrangements of ring ether groups at the edges of the mrGO when annealed at 600 °C (see Fig. 3a, area II and III). Such rebuilt ether groups from the basal plane position to the edge position resulted in elevated peroxide formation activity.[37] Besides, the other oxygen group, –COOH, was experimentally confirmed as an active site for 2e$^-$ ORR. Chemical titration experiments using PH, BA, and 2-BrPE as titrants to specifically react with the C═O, C–OH, and COOH groups, respectively, were performed to identify the 2e$^-$ ORR active sites.[17] The results indicated that the COOH groups on the carbon sheet contributed most to the 2e$^-$ ORR performance, and DFT calculations demonstrated that the COOH on the edge (see Fig. 3a, area IV) has the highest catalytic activity towards 2e$^-$ ORR. These studies have thoroughly investigated the types of oxygen groups and their geometric positions on the graphene base, which implies that the precise design of catalysts significantly affects the 2e$^-$ ORR performance.

In addition to the O dopant, the nitrogen (N) dopant is also widely studied for 2e$^-$ ORR due to the big difference in electronegativity between the nitrogen atom and carbon atom. Regarding nitrogen-doped carbonaceous materials, the main active sites contain pyridinic, pyrrolic, and graphitic N (see Fig. 3b). The pyridinic N has a lone pair of electrons, which implies it can be easily reduced or protonated, especially in acidic electrolytes.[40] Such a characteristic hinders the capacity to attenuate the O–O bond, resulting in a predisposition towards the formation of H_2O_2. However, in neutral or alkaline pH environments, there was a notable reduction in selectivity for H_2O_2, which can be attributed to the enhanced feasibility of water (H_2O) generation *via* the cleavage of the O–O bond. Consequently, carbons dominated by pyridinic sites demonstrated enhanced performance in the 2e$^-$ ORR within acidic electrolytes.[41] Nevertheless, both pyrrolic N and graphitic N also demonstrated their catalytic activity towards the 2e$^-$ ORR. Specifically, the catalytic activity in pyrrolic N-dominated carbons arises from the positive charge on the adjacent carbon, induced by the high electronegativity of the pyrrolic N within the carbon network.[7,42] In the case of graphitic nitrogen, it donates electrons to the π-conjugated system of carbon–carbon bonds, thereby facilitating the adsorption of molecular oxygen. This electron donation subsequently leads to a proton-coupled electron transfer, facilitating the formation of the *OOH intermediate species.[43] In addition to the most widely explored O and N dopants, other non-metallic elements including boron (B), fluorine (F), phosphorus (P), and sulfur (S) were introduced into the carbon base to enhance the 2e$^-$ ORR performance.[35,40,44–48]

Moreover, the incorporation of metallic dopants has significantly attracted the interest of researchers. This heightened focus is largely attributed to the comparatively limited catalytic activity of non-metallic dopants within carbon-based frameworks, despite their pronounced selectivity for H_2O_2 production. Recent research has delved into highly active single-atom catalysts, which are composed of atomically dispersed metals and substrates. This category encompasses non-precious metals like Fe, Co, Ni, and Mn,[49–53] as well as precious metals such as Pt, Os, Ir, Rh, Ru, and Pd.[20,54–56] Generally, the active metallic atoms (M) are combined with nitrogen atoms, as shown in Fig. 3c, to construct M–N*x* sites on the carbon substrates. According to the DFT calculations shown in Fig. 3d, many metals, for example, nickel (Ni) and silver (Ag) exhibit a preference for producing H_2O_2 rather than H_2O compared to metals like ruthenium (Ru), iron (Fe), and cobalt (Co), which is attributed to their enhanced protophilic properties for H_2O_2 production. While for the Ru, Fe, and Co active metal centers, their preference lies in breaking the *OOH intermediates to *O, which leads to H_2O formation. Based on the calculated volcano plot, almost no active M–N_4 sites are close to the ideal volcano plot for H_2O_2 production (ΔG_{OOH^*} = 4.22 eV). It is beneficial to subtly adjust the M–N_4 site to retain most of its significant catalytic efficiency in the generation of H_2O_2. Optimization of the synergy between the metal center and the surrounding atomic configuration, coupled with alterations to the metal center of the M–N_4 moiety, is necessary to achieve the desired ΔG_{OOH^*} value and enhance the production of H_2O_2. For example, the Co–N_4 moiety can be tailored by fine-tuning its surrounding oxygen atomic configuration; as shown in Fig. 3d, the new site Co–N_4(O), incorporated in nitrogen-doped graphene (NG), demonstrated optimized H_2O_2 production.[51] Besides, atomic Co–N*x*–C sites on oxygen group-functionalized carbons, denoted as Co–POC–O, were synthesized through the processes of pyrolysis and oxidation of a cobalt-coordinated porphyrin framework precursor, demonstrating remarkable performance in the electrochemical synthesis of H_2O_2.[49] Interestingly, Yijin Kang *et al.* found that the pyrrole-type Co–N_4 primarily facilitates the 2e$^-$ ORR, whereas the pyridine-type Co–N_4 is instrumental in the 4e$^-$ ORR (Fig. 3c). Significantly, the pyrrole-type Co–N_4 exhibited a remarkable H_2O_2 selectivity of 94% under acidic conditions. The observed enhancement in catalytic performance is ascribed to a diminished interaction between O_2 and the reactive intermediate *OOH, thereby augmenting H_2O_2 production.[52] Additionally, subsequent research has demonstrated that incorporating a second cobalt atom into the Co–N_4 coordination to create novel diatomic cobalt sites, as illustrated in Fig. 3e, attenuates the binding affinity of *OOH and *HOOH.[57] These newly engineered diatomic cobalt sites thus inhibit the cleavage of the O–O bond while concurrently mitigating the parasitic hydrogen peroxide reduction reaction (H_2O_2RR). Although atomically dispersed metals on carbon substrates are mostly reported, for example, CuS_x and titanium nitride, they can be

used as substrates to load active atoms for H_2O_2 production, in which the active atoms are surrounded by other metallic atoms or nonmetallic atoms (Fig. 3f).[20,55] Fabrication of hollow nanospheres by atomically dispersing platinum (Pt) on an amorphous CuS_x support (h-Pt1-CuS_x), featuring a substantial concentration of single atomic Pt sites (24.8 at%), was reported (Fig. 3f).[20] The active Pt atoms facilitate the activation of the inert CuS_x substrate, while CuS_x concurrently prevents the aggregation of Pt atoms. This novel catalyst demonstrates a high ability to consistently convert O_2 into H_2O_2 with selectivity ranging between 92% and 96% across a broad potential window of 0.05 to 0.7 V *vs.* RHE in $HClO_4$ electrolyte (Fig. 3g and h). Moreover, an electrochemical device capable of directly synthesizing H_2O_2 from H_2 and O_2 was developed, achieving H_2O_2 production rates as high as 546 ± 30 mol kg_{cat}^{-1} h^{-1} (Fig. 3i and j).

4.3 Metal hybridization engineering

Metallic catalysts, such as Pt and Pd, demonstrate notable catalytic efficiency in ORR, while predominantly facilitating the four-electron ($4e^-$) pathway.[6] The strategic design of an active metallic catalyst capable of suppressing the $4e^-$ pathway while promoting the $2e^-$ pathway holds substantial importance. Hence, gaining an in-depth understanding of the interactions between molecular oxygen (O_2) and the catalytic surface is crucial for the development of effective catalysts. As elucidated in ''Section 2: Reaction mechanisms of H_2O_2 production *via* $2e^-$ ORR,'' the protonation of O_2 to form *OOH intermediates represents a significant hurdle in the $2e^-$ ORR process. Therefore, the initial step for the $2e^-$ ORR is when the adsorbed O_2 on the catalytic surface captures a proton to form *OOH. The adsorption of O_2 manifests in two distinct configurations: dissociative side-on adsorption and associative end-on adsorption.[58] Fig. 4a and b illustrate that the side-on adsorption mechanism extends the bond length and attenuates the double bond in O_2, yielding H_2O as the product. However, the end-on adsorption mechanism leads to the adsorption of oxygen in the form of *OOH, which is capable of producing both H_2O_2 and H_2O. Therefore, the principal challenge in the design of $2e^-$ ORR catalysts lies in altering the O_2 adsorption mode from a ''side-on'' to an ''end-on'' configuration. To effectuate the transition from a ''side-on'' to an ''end-on'' adsorption configuration, two strategic approaches are proposed: (i) surface poisoning/shielding, which involves the deliberate obstruction of exposed ensemble sites with inert species (Fig. 4c), effectively altering the surface chemistry to favor ''end-on'' adsorption; and (ii) the alloying of the active metal with an inert metal, which facilitates the isolation of active metal atoms (Fig. 4c), thereby providing a distinct geometric arrangement conducive to the desired adsorption mode.

Partial occlusion of the active metal surface can be achieved through the employment of specific poisonous ions, including Cl^-, SCN^-, CN^-, Br^- and S^{2-}, as well as other entities such as amorphous carbon, TiO_2, *etc.*, to enhance H_2O_2 selectivity.[1,6] Introducing cyanide ions (CN^-) into the H_2SO_4 electrolyte modifies the ORR selectivity towards the $2e^-$ pathway while reducing the overall ORR activity (Fig. 4d).[59] This modification can be attributed to changes in the configuration of species adsorbed on the Pt surfaces of the Pt(111) catalyst. Besides, other ions, for example, Cl^-, Br^-, and S^{2-} were also found to poison the Pt site in acidic electrolytes due to their strong adsorption ability.[60–62] Although ion poisoning can effectively facilitate the $2e^-$ ORR pathway, the introduction of heteroatom ions into electrolytes and reduced overall activity of the catalysts remain the challenge. Therefore, the direct design of active materials with ''self-shielding'' characteristics for enhanced $2e^-$ ORR performance is another effective strategy. These ''self-shielding'' materials are designed based on the principle of changing the ''side-on'' type to the ''end-on'' type. For example, when Pt nanoparticles were coated with an amorphous carbon layer (ACL), as shown in Fig. 4b, it was observed that the composite of Pt@ACL facilitated the adsorption of O_2 in an end-on configuration, significantly improving the performance of H_2O_2 electrosynthesis.[58] Importantly, the catalyst demonstrated enhanced catalytic stability, which is likely attributed to the shielding of Pt catalysts by the carbon layers enveloping them. This protective mechanism effectively mitigates the risks of leaching and ripening under conditions of high corrosivity during operation.[58] Similarly, Markovic *et al.* reported a Pt(111) catalyst enveloped by a calix[4]arene. Because of the strong inhibition of O_2 adsorption and reduced exposure of Pt sites, the ORR activity on such catalysts is reduced with the concomitant formation of H_2O_2.[63] Furthermore, an intriguing category of support effect, which leverages the advantages of encapsulation, is the strong metal–support interaction.[64] As shown in Fig. 4e, the TiO_{2-x}/Pd/TiO_2 sample was prepared by using an unprecedented time-dependent mechanical milling method. During this process, the TiO_2 substrate was reduced to TiO_{2-x} overlayers and coated with Pd nanoparticles (Pd NPs). This process facilitated a valence band restructuring and a reduction in the d-band center of the surface Pd atoms, significantly influencing the electronic and geometric properties of the catalyst. These alterations led to optimized adsorption energies of OOH* intermediates. A progressive decrease in the limiting current density of the disk current, accompanied by an augmentation in the ring current, was discernible from the 0.5 h-Pd/TiC to the 6 h-Pd/TiC samples. This trend suggests a transition from the $4e^-$ ORR pathway to the $2e^-$ ORR pathway (Fig. 4f). The augmentation in the faradaic efficiency of H_2O_2 production, escalating from approximately 35% to exceed 90%, substantiates this observation (Fig. 4g).

Analogous to the surface poisoning/shielding strategy, which modulates the performance by altering the direct contact interface between the catalytic sites and O_2, metallic alloying, which involves combining an active metal with an inert metal that exhibits weak interaction with O_2, can isolate the highly active metals (For example, Pt and Pd dominate the $4e^-$ ORR pathway), and alter the adsorption geometry of the O_2 molecule. For example, noble metals and their alloys, such as Pd–Au,[65,66] and Pd–Hg,[67,68] are currently state-of-the-art catalysts that demonstrate near-zero overpotential for oxygen reduction along with an

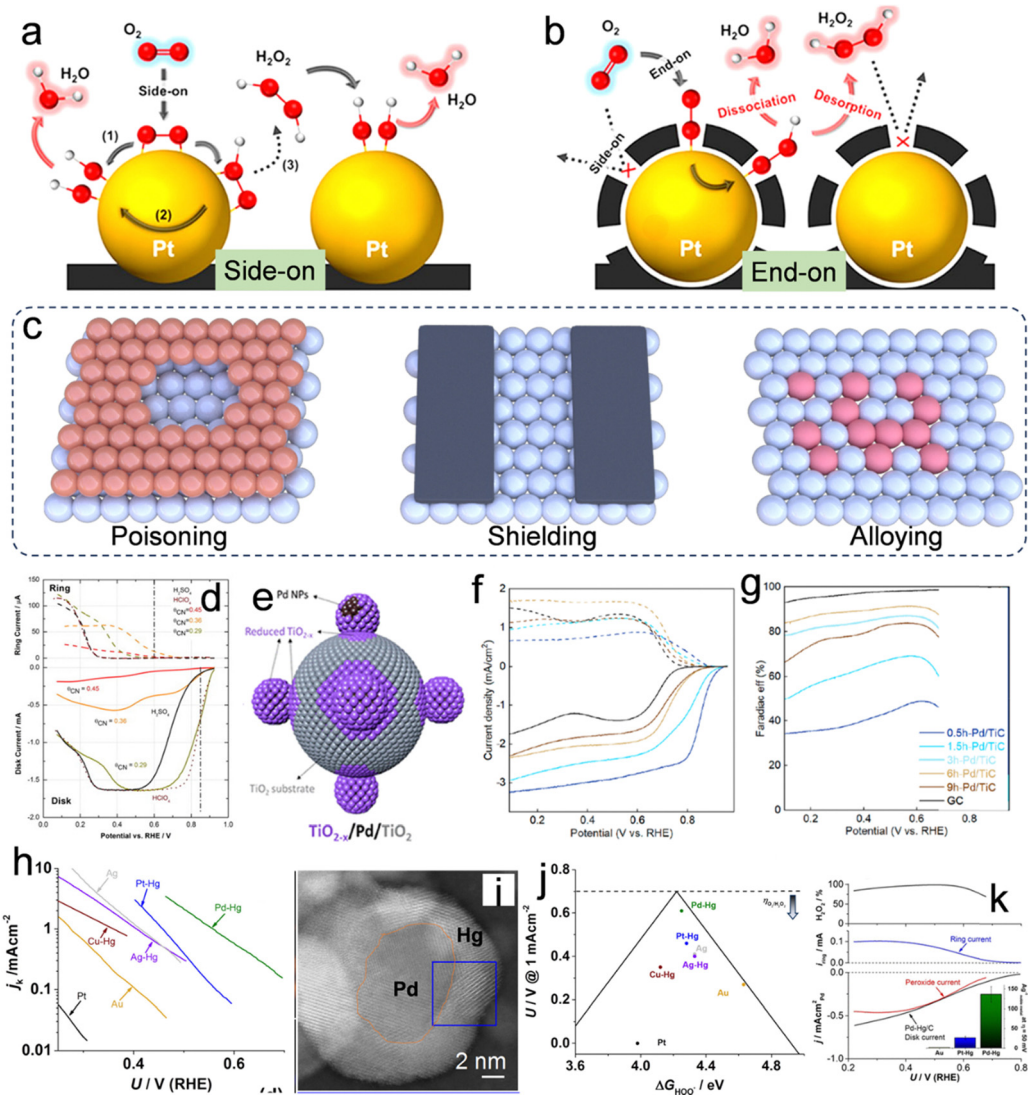

Fig. 4 O_2 adsorption on Pt/C and C(Pt)/C in the form of (a) side-on configuration and (b) end-on configuration. Reproduced from ref. 58. Copyright (2014) American Chemical Society. (c) Illustration of surface poisoning and shielding on the surface of the metal and metallic alloying. (d) Polarization curves obtained from RRDE experiments for the ORR on a Pt (111)–CN_{ad} electrode with varying CN_{ad} coverages, conducted in a 0.05 M H_2SO_4 solution. Reproduced from ref. 59. Copyright (2015) Elsevier. (e) Illustrative schematic demonstrating the encapsulation process of a TiO_{2-x} overlayer on Pd NPs *via* ball milling. (f) LSV curves obtained using an RRDE and corresponding (g) Faraday efficiency for the production of H_2O_2. Reproduced from ref. 64. Copyright (2022) American Chemical Society. (h) Kinetic current density for H_2O_2 as a function of the applied potential. (i) TEM images of the prepared Pd-Hg alloy. (j) The potential needed to achieve a kinetic current density of 1 mA cm^{-2} for H_2O_2 on polycrystalline catalysts as a function of the calculated *OOH binding energy. (k) LSV curves obtained using an RRDE and corresponding H_2O_2 selectivity. Reproduced from ref. 68. Copyright (2014) American Chemical Society.

extremely high H_2O_2 selectivity of up to 98%. For example, Au NPs embellished with Pd atoms have exhibited an augmented production of H_2O_2. Through an investigation into the influence of Pd content on the Au surface, it was discerned that Pd does not segregate on the Au NP surface until its concentration surpasses 8%; at this point the selectivity for H_2O_2 production can reach 95% in 0.1 M $HClO_4$.[69] Nevertheless, an excessive concentration of Pd leads to the formation of Pd ensemble sites, which preferentially dissociate the oxygen bond (O–O), thereby diminishing the selectivity for H_2O_2 production. Subsequent research has revealed that isolating Rh, Pd, Pt, or Rh sites on Au (111) surfaces enhances the performance of the $2e^-$ ORR relative to pure gold.[70]

Furthermore, E. L. Stephens systematically studied the non-noble metallic Hg alloys for $2e^-$ ORR.[68] As shown in Fig. 4h, the curves delineating the partial current densities associated with hydrogen peroxide production, relative to the applied potential, were plotted. The findings underscore the critical impact of catalyst composition on the requisite overpotential. Remarkably, the Pd–Hg alloy demonstrated the highest current at minimal overpotential. However, Pt–Hg, Ag–Hg, and Cu–Hg demonstrated a sequential escalation in overpotential. The Pd–Hg alloy exhibits a core–shell configuration, wherein Pd constitutes the core and Hg forms the shell, as illustrated in Fig. 4i. According to density functional theory (DFT) calculations presented in Fig. 4j, the Pd–Hg

alloy is positioned near the apex of the volcano plot, demonstrating the minimum overpotential or heightened catalytic activity. The LSV curves shown in Fig. 4k further confirm the high H_2O_2 selectivity, surpassing 95% within the voltage window of 0.35 to 0.55 V *vs.* RHE in 0.1 M $HClO_4$.

5. Designing setups for H_2O_2 production

To realize industrial production of H_2O_2 *via* the electrochemical synthetic strategy, rationally designing setups is another crucial engineering aspect that aims to achieve an efficient device for stable H_2O_2 products. Therefore, the designed setup should maintain the original active sites for oxygen adsorption, ensure effective mass migration, facilitate excellent H_2O_2 desorption and exhibit good stability.[71]

Although the commonly used RRDE method can maximize the advantages of a catalyst, the H_2O_2 production is so limited that it greatly hinders the industrial production. The one-pot configuration, depicted in Fig. 5a, employs the catalyst-coated carbon cloth directly as the working electrode, alongside a graphite rod serving as the counter electrode and an additional reference electrode.[11] The operational conditions for this setup closely mimic those of the RRED system. Li *et al.* studied H_2O_2 production using this one-pot setup reactor. In this system, the production rate of H_2O_2 reached 115.32 mmol $(g_{cat}\ h)^{-1}$ at 0.5 V *vs.* RHE, and the Faraday efficiency (FE) reached 89.0%.[11] However, the generated H_2O_2 is present throughout the electrolyte, which can be decomposed on the anode surface.[72] Nevertheless, an effective approach to prevent the decomposition of H_2O_2 at the anode involves coupling it with an anode that possesses a hydrogen oxidation reaction (HOR) functionality, capable of oxidizing H_2O into H_2O_2. In a recent study, Xia *et al.*[73] elucidated the elevated efficiency of a membrane-free flow cell designed for the electrocatalytic production of H_2O_2. They observed a significant increase in FE to 200%. This remarkable enhancement is attributed to the application of hydrophilic carbon fiber paper, which functions dually as both the cathode and the anode, facilitating the concurrent generation of H_2O_2. An alternative strategy to mitigate the decomposition of H_2O_2 at the anode involves employing a membrane to segregate the cathode and anode chambers. In a similar study, Yamanaka *et al.* conducted a study on H_2O_2 production using an H-cell in a one-pot batch reactor (Fig. 5b), where they noted a pronounced degradation in H_2O_2 electrosynthesis efficiency in comparison to experiments conducted in an H-cell equipped with a membrane.[72] The integration of a membrane within the H-cell effectively precludes the migration of H_2O_2 to the anode; however, the increased separation between the cathode and the anode results in an elongated ion diffusion path, thereby escalating solution resistance. Additionally, the limited

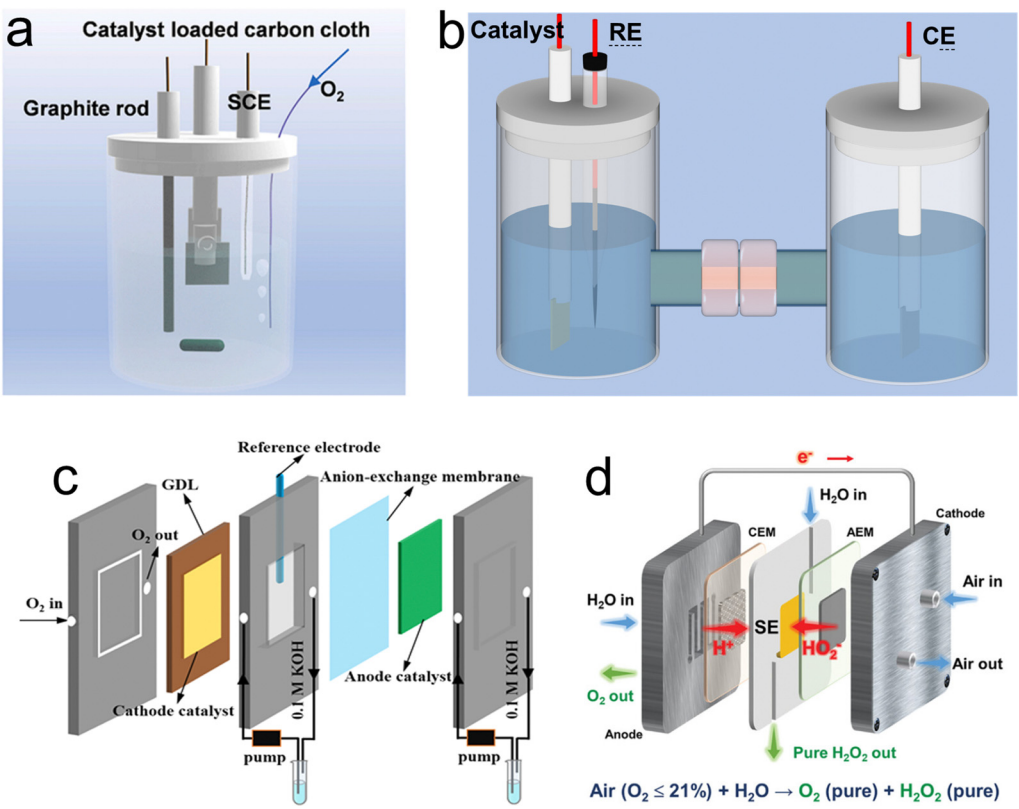

Fig. 5 Different types of setups for H_2O_2 production. (a) One-pot setup. Reproduced from ref. 11. Copyright (2022) Elsevier. (b) H-cell. (c) Illustration of the flow cell setup. Reproduced from ref. 17. Copyright (2021) Wiley-VCH GmbH. (d) solid–electrolyte (SE) cell system. Reproduced from ref. 78. Copyright (2023) Wiley-VCH GmbH.

solubility of O_2 in liquid electrolytes further constrains the maximum rate of H_2O_2 production achievable. Furthermore, the discontinuous nature of H-cells and the accumulation of H_2O_2 on the electrode surface leads to further reduction of H_2O_2.

To address the drawbacks of the one-pot setup and H-cell, gas-diffusion electrodes (GDEs) were developed by integrating a hydrophobic layer (gas-diffusion layer, GDL) and catalysts, as shown in Fig. 5c.[17] The GDEs are meticulously engineered by coating the catalyst onto the gas diffusion layer, establishing three-phase interfaces (TPIs) when immersed in the electrolyte. The TPIs play a crucial role in ensuring the efficient transport of O_2, thereby maintaining a consistent flow of O_2 directly to the catalyst layer.[74–77] This configuration is instrumental in optimizing the efficacy of the electrode by ensuring that the catalytic sites are uniformly accessible to O_2. Through this strategic layering and interface design, the GDEs achieve a delicate balance between oxygen permeability and catalytic activity, thereby maximizing the overall performance of catalytic electrodes in H_2O_2 production. Utilizing this apparatus, the oxygen-doped carbon nanosheet (OCNS900) was affixed onto the gas diffusion layer (GDL) to fabricate the cathode for the oxygen reduction reaction (ORR), while an iridium dioxide (IrO_2)-coated titanium sheet was employed as the anode for the oxygen evolution reaction (OER). The rate of H_2O_2 production was quantified to be 770 mmol g(catalyst h)$^{-1}$ following an operational period of 1 hour.[17] Interestingly, for the electrosynthesis of pure H_2O_2 solution, a solid–electrolyte (SE) cells system was constructed (Fig. 5d), avoiding the need for expensive and intricate post-treatment processes necessary for purifying H_2O_2 solutions in conventional setups illustrated in Fig. 5a–c. For example, both an anion exchange membrane (AEM) and a proton exchange membrane (PEM), specifically Nafion 117, were employed to facilitate anion and cation exchange, respectively. The poly(styrene-*co*-divinylbenzene) ion-exchange resin sulfonate (HEOWNS, P-72091, 75-200 mesh) was utilized as the solid electrolyte (SE). The cathode and anode sides were supplied with airflow and deionized water, respectively.[78] Chuangang Hu and colleagues utilized N and S co-doped TCNTs (N,S-TCNTs) as cathode catalysts to achieve a high FE of 95.1% at a current density of 150 mA cm^{-2}. Concurrently, at a current density of 300 mA cm^{-2}, the highest production rate of 4.35 mmol cm^{-2} h^{-1} can be achieved.[78]

6. Conclusions and perspectives

In this review, an exhaustive summary of various engineering strategies aimed at identifying efficient 2e$^-$ ORR catalysts has been provided. This summary encapsulates discussions on microstructure engineering, heteroatom doping, and metal hybridization techniques. A 3D ordered mesopore structure is regarded as an efficient configuration for a good 2e$^-$ ORR catalyst as it increases the exposure of active sites and facilitates mass transport of H_2O_2. Besides, heteroatom doping is commonly used to guide the design of active sites, particularly in the field of carbonaceous materials. The inert atoms on the substrates are activated after the incorporation of heteroatoms (For example, B, N, O, F, and P) *via* regulating the local electronic structure and introducing active functional groups, thus inducing an enhanced 2e$^-$ ORR performance. Metal hybrid engineering, particularly involving noble metals such as Pt and Pd that are recognized for yielding highly active components for the 4e$^-$ ORR, is also used to induce a 2e$^-$ pathway *via* the utilization of poisoning/shielding and alloying. Transforming the O_2 adsorption configuration from ''side-on'' to ''end-on'' on the metallic surface can leverage the geometric effects of the catalyst for H_2O_2 production. In addition, the setups including the one-pot setup, H-cell, flow cell setup and solid–electrolyte (SE) cell for large-scale H_2O_2 production are also discussed. Considerable attention has been dedicated to the engineering of catalysts and electrochemical reactors. Despite noteworthy progress, the scaling up of H_2O_2 electrochemical production remains nascent compared to the traditional anthraquinone process. Consequently, this area presents both challenges and opportunities for the industrial production of H_2O_2 *via* 2e$^-$ ORR.

The development of efficient 2e$^-$ ORR catalysts that exhibit both high activity and selectivity remains a formidable challenge. Among the most extensively studied heteroatom-doped carbonaceous materials, an increase in selectivity typically coincides with a reduction in activity. Although the incorporation of metallic atoms into carbonaceous substrates has been shown to enhance the activity of H_2O_2 production up to a certain extent, it invariably leads to a compromise in H_2O_2 selectivity. More critically, a catalyst recognized for its superior 2e$^-$ ORR performance often exhibits a lower half-wave potential compared to its counterpart favored for 4e$^-$ ORR performance, suggesting that greater energy input is required to facilitate the electrosynthesis process. Additionally, although noble metallic alloys have shown high activity and selectivity, their high cost significantly limits their application on a large scale. Therefore, a profound understanding of the mechanisms governing the 2e$^-$ ORR is urgently required. Recent investigations have leveraged advanced *in situ* techniques, such as operando ATR-IR spectroscopy, *in situ* X-ray absorption near edge structure (XANES), *in situ* Raman spectroscopy, and density functional theory (DFT) calculations. These methodologies offer novel perspectives on pinpointing active sites and elucidating the structural evolution of catalysts. Such insights are paramount for the rational design of efficacious 2e$^-$ ORR catalysts.

Looking ahead, there is anticipation for the exploration of single-atom catalysts on low-cost substrates combined with simple preparation processes that ensure high activity, high selectivity, and affordability. Given that these catalysts will ultimately be used for large-scale H_2O_2 production, the integration of catalysts and reactors is also crucial. The methods for depositing these catalysts onto substrates need to be refined through techniques such as air spraying, ultrasonic spraying, and *in situ* growth, to ensure optimal ion/electron/mass transfer and gas flow. A reaction chamber that is resistant to the electrolyte and has a rational flow channel configuration,

maximizing the conversion rate of O_2, is vital for the electrosynthesis process. Therefore, there is a pressing need for focused efforts towards the development of reactors that not only offer superior catalytic performance but also possess chambers with excellent corrosion resistance.

In addition to the catalysts discussed above for H_2O_2 production, the electrolyte should also be focused on. Electrolytes provide the environments for the oxygen reduction reaction, which may affect the stability of the intermediate *OOH and finally regulate the H_2O_2 production. For example, Wu *et al.* found that cetyltrimethylammonium bromide (CTAB) can accelerate the $2e^-$ ORR performance of carbon black (CB) in 0.1 M KOH electrolyte, while sodium dodecylsulfate (SDS) weakened the $2e^-$ ORR performance due to the "pull-off" effect of the cationic surfactant.[79] Furthermore, P. Strasser *et al.* observed notable cation (K^+)-induced electrocatalytic enhancement effects on the $2e^-$ ORR in acidic environments.[80] In basic electrolytes, cations such as Cs^+, K^+, and Li^+ enhance the $2e^-$ ORR performance of oxygen-functionalized carbon in accordance with the ionic size of the cation: $Cs^+ > K^+ > Li^+$.[81] Therefore, rationally exploring the additives for the electrolyte is of great importance.

Author contributions

Ao Yu: writing, review and editing – original draft. Shengwen Liu – review and editing. Yang Yang: supervision, funding acquisition, project administration.

Conflicts of interest

We declare that we have no financial and personal relationships with other people or organizations that can inappropriately influence our work, and there is no professional or other personal interest of any nature or kind in any product, service, and/or company that could be construed as influencing the position presented in, or the review of, the manuscript entitled.

Acknowledgements

Y. Y. acknowledges the financial support from the National Science Foundation under grant no. CBET-1949840 and ACS PRF (65481-ND10). A. Y. and S. L. acknowledge the financial support from the Preeminent Postdoctoral Program (P3) at UCF.

References

1 J. H. Kim, Y.-T. Kim and S. H. Joo, *Curr. Opin. Electrochem.*, 2020, **21**, 109–116.
2 K. Dong, Y. Lei, H. Zhao, J. Liang, P. Ding, Q. Liu, Z. Xu, S. Lu, Q. Li and X. Sun, *J. Mater. Chem. A*, 2020, **8**, 23123–23141.
3 T. Lian, C. Huang, F. Liang, X. Li and J. Xi, *ACS Appl. Mater. Interfaces*, 2019, **11**, 45692–45701.
4 N. Wang, S. Ma, P. Zuo, J. Duan and B. Hou, *Adv. Sci.*, 2021, **8**, 2100076.
5 K. Mase, M. Yoneda, Y. Yamada and S. Fukuzumi, *Nat. Commun.*, 2016, **7**, 11470.
6 X. Huang, M. Song, J. Zhang, T. Shen, G. Luo and D. Wang, *Nano-Micro Lett.*, 2023, **15**, 86.
7 A. Byeon, W. C. Yun, J. M. Kim and J. W. Lee, *Chem. Eng. J.*, 2023, **456**, 141042.
8 D. W. Flaherty, *ACS Catal.*, 2018, **8**, 1520–1527.
9 Q. Liu, J. C. Bauer, R. E. Schaak and J. H. Lunsford, *Appl. Catal., A*, 2008, **339**, 130–136.
10 R. J. Lewis and G. J. Hutchings, *ChemCatChem*, 2019, **11**, 298–308.
11 A. Yu, G. Ma, L. Zhu, R. Zhang, Y. Li, S. Yang, H.-Y. Hsu, P. Peng and F.-F. Li, *Appl. Catal. B*, 2022, **307**, 121161.
12 A. Yu, G. Ma, L. Zhu, Y. Hu, R. Zhang, H.-Y. Hsu, P. Peng and F.-F. Li, *Nanoscale*, 2021, **13**, 15973–15980.
13 Z. Y. Lu, G. X. Chen, S. Siahrostami, Z. H. Chen, K. Liu, J. Xie, L. Liao, T. Wu, D. C. Lin, Y. Liu, T. F. Jaramillo, J. K. Nørskov and Y. Cui, *Nat. Catal.*, 2018, **1**, 156–162.
14 X. Zhang, X. Zhao, P. Zhu, Z. Adler, Z.-Y. Wu, Y. Liu and H. Wang, *Nat. Commun.*, 2022, **13**, 2880.
15 Q. Zhang, X. Tan, N. M. Bedford, Z. Han, L. Thomsen, S. Smith, R. Amal and X. Lu, *Nat. Commun.*, 2020, **11**, 4181.
16 S. Chen, Z. Chen, S. Siahrostami, D. Higgins, D. Nordlund, D. Sokaras, T. R. Kim, Y. Liu, X. Yan, E. Nilsson, R. Sinclair, J. K. Norskov, T. F. Jaramillo and Z. Bao, *J. Am. Chem. Soc.*, 2018, **140**, 7851–7859.
17 S. Chen, T. Luo, K. Chen, Y. Lin, J. Fu, K. Liu, C. Cai, Q. Wang, H. Li, X. Li, J. Hu, H. Li, M. Zhu and M. Liu, *Angew. Chem., Int. Ed.*, 2021, **60**, 16607–16614.
18 G. Chen, J. Liu, Q. Li, P. Guan, X. Yu, L. Xing, J. Zhang and R. Che, *Nano Res.*, 2019, **12**, 2614–2622.
19 Y. Pang, K. Wang, H. Xie, Y. Sun, M.-M. Titirici and G.-L. Chai, *ACS Catal.*, 2020, **10**, 7434–7442.
20 R. Shen, W. Chen, Q. Peng, S. Lu, L. Zheng, X. Cao, Y. Wang, W. Zhu, J. Zhang, Z. Zhuang, C. Chen, D. Wang and Y. Li, *Chem*, 2019, **5**, 2099–2110.
21 S. Wang, H. Liu, D. Ye, Q. Lan, X. Zhu, Y. Yang, R. Chen and Q. Liao, *Sep. Purif. Technol.*, 2022, **289**, 120687.
22 J. Park, Y. Nabae, T. Hayakawa and M.-A. Kakimoto, *ACS Catal.*, 2014, **4**, 3749–3754.
23 S. Chen, Z. Chen, S. Siahrostami, T. R. Kim, D. Nordlund, D. Sokaras, S. Nowak, J. W. F. To, D. Higgins, R. Sinclair, J. K. Nørskov, T. F. Jaramillo and Z. Bao, *ACS Sustainable Chem. Eng.*, 2018, **6**, 311–317.
24 V. Čolić, S. Yang, Z. Révay, I. E. L. Stephens and I. Chorkendorff, *Electrochim. Acta*, 2018, **272**, 192–202.
25 H. He, S. Liu, Y. Liu, L. Zhou, H. Wen, R. Shen, H. Zhang, X. Guo, J. Jiang and B. Li, *Green Chem.*, 2023, **25**, 9501–9542.
26 D. Zhang, E. Mitchell, X. Lu, D. Chu, L. Shang, T. Zhang, R. Amal and Z. Han, *Mater. Today*, 2023, **63**, 339–359.
27 X. Guo, S. Liu, X. Wan, J. Zhang, Y. Liu, X. Zheng, Q. Kong and Z. Jin, *Nano Lett.*, 2022, **22**, 4879–4887.
28 G. Zhu, T. Chen, Y. Hu, L. Ma, R. Chen, H. Lv, Y. Wang, J. Liang, X. Li, C. Yan, H. Zhu, H. Liu, Z. Tie, Z. Jin and J. Liu, *Nano Energy*, 2017, **33**, 229–237.
29 D. H. Mok, S. Back and S. Siahrostami, *Angew. Chem., Int. Ed.*, 2024, e202404677.
30 H. Yang, N. An, Z. Kang, P. W. Menezes and Z. Chen, *Adv. Mater.*, 2024, 2400140.
31 Y. Pang, H. Xie, Y. Sun, M.-M. Titirici and G.-L. Chai, *J. Mater. Chem. A*, 2020, **8**, 24996–25016.
32 L. Jing, Q. Tian, W. Wang, X. Li, Q. Hu, H. Yang and C. He, *Adv. Energy Mater.*, 2024, 2304418.
33 L. Han, Y. Y. Sun, S. Li, C. Cheng, C. E. Halbig, P. Feicht, J. L. Hübner, P. Strasser and S. Eigler, *ACS Catal.*, 2019, **9**, 1283–1288.
34 D. San Roman, D. Krishnamurthy, R. Garg, H. Hafiz, M. Lamparski, N. T. Nuhfer, V. Meunier, V. Viswanathan and T. Cohen-Karni, *ACS Catal.*, 2020, **10**, 1993–2008.
35 Y. Xia, X. Zhao, C. Xia, Z.-Y. Wu, P. Zhu, J. Y. Kim, X. Bai, G. Gao, Y. Hu, J. Zhong, Y. Liu and H. Wang, *Nat. Commun.*, 2021, **12**, 4225.
36 N. Yang, L. Li, J. Li, W. Ding and Z. Wei, *Chem. Sci.*, 2018, **9**, 5795–5804.
37 H. W. Kim, M. B. Ross, N. Kornienko, L. Zhang, J. Guo, P. Yang and B. D. McCloskey, *Nat. Catal.*, 2018, **1**, 282–290.
38 G.-F. Han, F. Li, W. Zou, M. Karamad, J.-P. Jeon, S.-W. Kim, S.-J. Kim, Y. Bu, Z. Fu, Y. Lu, S. Siahrostami and J.-B. Baek, *Nat. Commun.*, 2020, **11**, 2209.

39 X. Lu, D. Wang, K.-H. Wu, X. Guo and W. Qi, *J. Colloid Interface Sci.*, 2020, **573**, 376–383.
40 V. Perazzolo, C. Durante, R. Pilot, A. Paduano, J. Zheng, G. A. Rizzi, A. Martucci, G. Granozzi and A. Gennaro, *Carbon*, 2015, **95**, 949–963.
41 D. Iglesias, A. Giuliani, M. Melchionna, S. Marchesan, A. Criado, L. Nasi, M. Bevilacqua, C. Tavagnacco, F. Vizza, M. Prato and P. Fornasiero, *Chem*, 2018, **4**, 106–123.
42 L. Li, C. Tang, Y. Zheng, B. Xia, X. Zhou, H. Xu and S.-Z. Qiao, *Adv. Energy Mater.*, 2020, **10**, 2000789.
43 J. Zhang, G. Zhang, S. Jin, Y. Zhou, Q. Ji, H. Lan, H. Liu and J. Qu, *Carbon*, 2020, **163**, 154–161.
44 K. Zhao, Y. Su, X. Quan, Y. Liu, S. Chen and H. Yu, *J. Catal.*, 2018, **357**, 118–126.
45 W. Wang, X. Lu, P. Su, Y. Li, J. Cai, Q. Zhang, M. Zhou and O. Arotiba, *Chemosphere*, 2020, **259**, 127423.
46 N. Jia, T. Yang, S. Shi, X. Chen, Z. An, Y. Chen, S. Yin and P. Chen, *ACS Sustainable Chem. Eng.*, 2020, **8**, 2883–2891.
47 H. Kim, H. Yang, J. Kang and N. Takeuchi, *Carbon*, 2021, **182**, 242–253.
48 Y. Sun, S. Li, B. Paul, L. Han and P. Strasser, *J. Electroanal. Chem.*, 2021, **896**, 115197.
49 B. Q. Li, C. X. Zhao, J. N. Liu and Q. Zhang, *Adv. Mater.*, 2019, **31**, e1808173.
50 Y. Sun, L. Silvioli, N. R. Sahraie, W. Ju, J. Li, A. Zitolo, S. Li, A. Bagger, L. Arnarson, X. Wang, T. Moeller, D. Bernsmeier, J. Rossmeisl, F. Jaouen and P. Strasser, *J. Am. Chem. Soc.*, 2019, **141**, 12372–12381.
51 E. Jung, H. Shin, B.-H. Lee, V. Efremov, S. Lee, H. S. Lee, J. Kim, W. Hooch Antink, S. Park, K.-S. Lee, S.-P. Cho, J. S. Yoo, Y.-E. Sung and T. Hyeon, *Nat. Mater.*, 2020, **19**, 436–442.
52 S. Chen, T. Luo, X. Li, K. Chen, J. Fu, K. Liu, C. Cai, Q. Wang, H. Li, Y. Chen, C. Ma, L. Zhu, Y.-R. Lu, T.-S. Chan, M. Zhu, E. Cortés and M. Liu, *J. Am. Chem. Soc.*, 2022, **144**, 14505–14516.
53 Y. Tian, M. Li, Z. Wu, Q. Sun, D. Yuan, B. Johannessen, L. Xu, Y. Wang, Y. Dou, H. Zhao and S. Zhang, *Angew. Chem., Int. Ed.*, 2022, **61**, e202213296.
54 C. H. Choi, M. Kim, H. C. Kwon, S. J. Cho, S. Yun, H.-T. Kim, K. J. J. Mayrhofer, H. Kim and M. Choi, *Nat. Commun.*, 2016, **7**, 10922.
55 S. Yang, J. Kim, Y. J. Tak, A. Soon and H. Lee, *Angew. Chem., Int. Ed.*, 2016, **55**, 2058–2062.
56 J. H. Kim, D. Shin, J. Lee, D. S. Baek, T. J. Shin, Y.-T. Kim, H. Y. Jeong, J. H. Kwak, H. Kim and S. H. Joo, *ACS Nano*, 2020, **14**, 1990–2001.
57 H. Huang, M. Sun, S. Li, S. Zhang, Y. Lee, Z. Li, J. Fang, C. Chen, Y.-X. Zhang, Y. Wu, Y. Che, S. Qian, W. Zhu, C. Tang, Z. Zhuang, L. Zhang and Z. Niu, *J. Am. Chem. Soc.*, 2024, **146**(13), 9434–9443.
58 C. H. Choi, H. C. Kwon, S. Yook, H. Shin, H. Kim and M. Choi, *J. Phys. Chem. C*, 2014, **118**, 30063–30070.
59 E. G. Ciapina, P. P. Lopes, R. Subbaraman, E. A. Ticianelli, V. Stamenkovic, D. Strmcnik and N. M. Markovic, *Electrochem. Commun.*, 2015, **60**, 30–33.
60 V. Stamenkovic, N. M. Markovic and P. N. Ross, *J. Electroanal. Chem.*, 2001, **500**, 44–51.
61 N. M. Marković, H. A. Gasteiger, B. N. Grgur and P. N. Ross, *J. Electroanal. Chem.*, 1999, **467**, 157–163.
62 D. He, L. Zhong, S. Gan, J. Xie, W. Wang, Z. Liu, W. Guo, X. Yang and L. Niu, *Electrochim. Acta*, 2021, **371**, 137721.
63 B. Genorio, D. Strmcnik, R. Subbaraman, D. Tripkovic, G. Karapetrov, V. R. Stamenkovic, S. Pejovnik and N. M. Marković, *Nat. Mater.*, 2010, **9**, 998–1003.
64 J. Zhang, J. Ma, T. S. Choksi, D. Zhou, S. Han, Y.-F. Liao, H. B. Yang, D. Liu, Z. Zeng, W. Liu, X. Sun, T. Zhang and B. Liu, *J. Am. Chem. Soc.*, 2022, **144**, 2255–2263.
65 J. K. Edwards, S. J. Freakley, R. J. Lewis, J. C. Pritchard and G. J. Hutchings, *Catal. Today*, 2015, **248**, 3–9.
66 E. Pizzutilo, S. J. Freakley, S. Cherevko, S. Venkatesan, G. J. Hutchings, C. H. Liebscher, G. Dehm and K. J. J. Mayrhofer, *ACS Catal.*, 2017, **7**, 5699–5705.
67 S. Siahrostami, A. Verdaguer-Casadevall, M. Karamad, D. Deiana, P. Malacrida, B. Wickman, M. Escudero-Escribano, E. A. Paoli, R. Frydendal, T. W. Hansen, I. Chorkendorff, I. E. Stephens and J. Rossmeisl, *Nat. Mater.*, 2013, **12**, 1137–1143.
68 A. Verdaguer-Casadevall, D. Deiana, M. Karamad, S. Siahrostami, P. Malacrida, T. W. Hansen, J. Rossmeisl, I. Chorkendorff and I. E. L. Stephens, *Nano Lett.*, 2014, **14**, 1603–1608.
69 J. S. Jirkovský, I. Panas, E. Ahlberg, M. Halasa, S. Romani and D. J. Schiffrin, *J. Am. Chem. Soc.*, 2011, **133**, 19432–19441.
70 J. S. Jirkovský, I. Panas, S. Romani, E. Ahlberg and D. J. Schiffrin, *J. Phys. Chem. Lett.*, 2012, **3**, 315–321.
71 Y. Tian, D. Deng, L. Xu, M. Li, H. Chen, Z. Wu and S. Zhang, *Nano-Micro Lett.*, 2023, **15**, 122.
72 I. Yamanaka and T. Murayama, *Angew. Chem., Int. Ed.*, 2008, **120**, 1926–1928.
73 C. Xia, S. Back, S. Ringe, K. Jiang, F. Chen, X. Sun, S. Siahrostami, K. Chan and H. Wang, *Nat. Catal.*, 2020, **3**, 125–134.
74 W. Sun, B. A. Peppley and K. Karan, *J. Power Sources*, 2005, **144**, 42–53.
75 P. J. Hamilton and B. G. Pollet, *Fuel Cells*, 2010, **10**, 489–509.
76 R. E. Rosli, A. B. Sulong, W. R. W. Daud, M. A. Zulkifley, T. Husaini, M. I. Rosli, E. H. Majlan and M. A. Haque, *Int. J. Hydrogen Energy*, 2017, **42**, 9293–9314.
77 N. Aukland, A. Boudina, D. S. Eddy, J. V. Mantese, M. P. Thompson and S. S. Wang, *J. Mater. Res.*, 2004, **19**, 1723–1729.
78 Y. Long, J. Lin, F. Ye, W. Liu, D. Wang, Q. Cheng, R. Paul, D. Cheng, B. Mao, R. Yan, L. Zhao, D. Liu, F. Liu and C. Hu, *Adv. Mater.*, 2023, **35**, 2303905.
79 K.-H. Wu, D. Wang, X. Lu, X. Zhang, Z. Xie, Y. Liu, B.-J. Su, J.-M. Chen, D.-S. Su, W. Qi and S. Guo, *Chem*, 2020, **6**, 1443–1458.
80 J. L. Hübner, L. E. B. Lucchetti, H. N. Nong, D. I. Sharapa, B. Paul, M. Kroschel, J. Kang, D. Teschner, S. Behrens, F. Studt, A. Knop-Gericke, S. Siahrostami and P. Strasser, *ACS Energy Lett.*, 2024, 1331–1338, DOI: **10.1021/acsenergylett.3c02743**.
81 J. Lee, J. S. Lim, G. Yim, H. Jang, S. H. Joo and Y. J. Sa, *ACS Appl. Mater. Interfaces*, 2021, **13**, 59904–59914.